RSC Advances

PAPER

View Article Online
View Journal | View Issue

Cite this: *RSC Adv.*, 2022, **12**, 1331

Prediction of intermediate band in Ti/V doped γ-In_2S_3†

R. Mariyal Jebasty,[a] Anja Olafsen Sjåstad [b] and R. Vidya *[a]

Received 23rd September 2021
Accepted 12th December 2021

DOI: 10.1039/d0ra08132a

rsc.li/rsc-advances

Materials with an intermediate energy band (IB) introduced in the forbidden gap are viable alternatives to tandem configurations of solar cells for increasing the photon-conversion efficiency. One of the aspiring designs proposed for the intermediate band concept is hyperdoped (Ti, V):In_2S_3. Being very important in copper indium gallium sulfide (CIGS) solar cells, indium thiospinel (In_2S_3) is known for its three different temperature as well as pressure, polymorphs. The most stable β-In_2S_3 was experimentally shown to have an isolated intermediate band (IB) and exhibits sub-band gap absorption due to the completely filled IB after V-doping. Though experimental observation holds a positive signature, recent DFT studies did not show a metallic intermediate band for the V dopant in the 3+ charge state. In order to clarify this, we have taken incentive from experimental XRD analysis that V-doped β-In_2S_3 shows peaks from disordered In vacancies (either α or γ), in addition to the ordered In vacancies expected. Hence, we have carried out state-of-the-art DFT based computations on pure and Ti, V-doped In_2S_3 in the γ-phase which has not been studied yet. We considered the Ti and V dopants in various charge states. Our theoretical study including hybrid functional, does in fact find the IB in V-doped γ-In_2S_3. However, at equilibrium the IB lies in between the Fermi level (E_F) and conduction band minimum (CBM).

1 Introduction

The imposing concept of an intermediate band gap (IB) was proposed by Luque and Martí[1] in 1997, as one of the methodologies to overcome the Shockley and Queisser (SQ) limit of efficiency of solar cells. Historically, the tandem cell with three-layers has been proposed for a high efficiency of about 49%.[2] However, a recently demonstrated 2D BAs/InTe tandem cell configuration reaches an experimental high photo conversion efficiency (PCE) of 30.2%.[4] Furthermore, the recently reported bulk perovskites/In_2S_3 based tandem cell reaches a maximum PCE of 18.83%.[5] Intermediate band gap solar cells (IBSCs) can potentially reach quantum efficiency of no more than 50% since the tandem cell requires two photons to emit one electron.[3] However, either a band gap or sub-band gap photon is enough to drop down an electron in the case of an ideal intermediate band gap semiconductor. The expected quantum efficiency of the IBSC model is 63.1% with the radiative bands.

Until now, the search for IB materials has been conducted mainly within the traditional semiconductors.[1–3] The IB feature has been identified in a few wide bandgap materials with specific dopants, as reported in selected theoretical and experimental studies.[6,7] Among the numerous theoretically proposed materials, special focus on wide band gap semiconductors with transition metal doping has received profound interest because of its metallic intermediate band.[8–16] In this series, indium thiospinel has been a recurring material for photo-voltaic cells operating with an intermediate band.[17–19] The interest over this material is stimulated due to its exotic surface chemistry in photocatalytic, photo-electrocatalytic applications,[20–22] and optoelectronic devices like thin film solar cells, battery materials, as well as in the photochemical cells because of its cyclicability, which explains the success of In_2S_3.[23–27]

Being a promising candidate for CIGS solar cells, indium thiospinel (In_2S_3) allows three different temperature modifications in addition to a pressure transition.[28–32] α-In_2S_3 is a low temperature polymorph, which takes a cubic-defect spinel structure of space group $Fd\bar{3}m$ with 1/3rd of tetrahedral indium sites remaining vacant.[33] Further, the vacancy is randomly distributed and the structure can be stabilized up to 400 K. The β-In_2S_3 crystallizes at room temperature in the defect spinel structure with 1/4 of tetrahedral hole (T_d) vacancies.[34] However, the vacancies are arranged in a 4_1 screw axis along the *c*-axis. This forms tetrahedral geometry of three cubes stacked along the *c*-axis. At 700 K temperature, the ordered spinel is transformed into disordered cubic-spinel (α-In_2S_3) and with excess In content, it can be stabilized at room temperature. Hahn and Klinger suggested that the ordering of the 'In' atom is the main difference between the α and β phases.[35]

[a]*Department of Medical Physics, Anna University, Sir C. V. Raman Advanced Science Block, Sardar Patel Road, Guindy, Chennai - 600 025, India. E-mail: vidyar@annauniv.edu*

[b]*Centre for Materials Science and Nanotechnology, Department of Chemistry, University of Oslo, PO Box 1033, N-0315 Oslo, Norway*

† Electronic supplementary information (ESI) available. See DOI: 10.1039/d0ra08132a

Further increases in temperature lead to complete rearrangement of atoms resulting in a new γ-In_2S_3, which is stable in the trigonal phase up to the melting point.[36] The γ-In_2S_3 is of reconstructive type and can be quenched at room temperature with substituted impurities.[33] The high pressure polymorph (ε-In_2S_3) is a special case of a trigonal γ-In_2S_3 with corundum structure with hexagonal close packing.[37] An unobtrusive change in physico-chemical properties will result based on the vacancy and ordered/disordered pattern of the In arrangement.[38] However, the role of vacancy ordering has not received much attention from the research community so far.

The room temperature β-In_2S_3 has received more attention compared to other phases, while few physical properties of the other phases are predicted with the aid of theoretical calculations.[25,39,40] Nevertheless, the theoretical formation energy of the various phases has not been studied yet. Even though the β and γ phases were shown to have the same ground state energy using the full potential linearized augmented planewave (FP-LAPW) method,[39] only the β-In_2S_3 has been focused on with no further analysis on properties of γ-In_2S_3.

Recently, the thermodynamic and kinetic factors analyzed by Horani and Lifshitz,[41] showed the structural transition of the γ to β phase. They exposed the less stable γ-phase as a room temperature polymorph in addition to the β-phase. Since the experimentally synthesized phases have not been studied yet for their bulk physical properties, Horani and Lifshitz alluded to the energy gap of nanoplatelets by correlating the electronic states of the bulk materials.

Notably for Ti:In_2S_3, a DFT study has shown that completely filled IB can be formed.[42] Furthermore, the predicted IBSC, V-doped In_2S_3 (V:In_2S_3) also underlined the ease of structural transition from the β to γ phase. The solution processed V:β-In_2S_3 led to the formation of less stable V:γ-In_2S_3 (trigonal).[43] But the doped sample is well crystallized having a quite similar band gap to that of β-In_2S_3. Notably, the electron paramagnetic resonance (EPR) signal at $g \approx 1.98$ indicates the formation of a superimposed hyper-fine structure. Also, the coexistence of α and β phases has been observed, and both are identified with IB formation by hyperdoping of vanadium since they have a spinel structure.[44] Due to the presence of doped impurities, a small transition pressure is enough to destabilize the β-phase. Upon increasing the dopant concentration the less stable γ-phase becomes stable.[45–47]

A recent study by Ghorbani *et al.*,[48] using the HSE functional has included the V-impurity in different charge states. They showed that V^{3+} does not introduce any IB, whereas the V^{2+} introduces an IB that is filled. Further increase in the dopant concentration was shown to decrease the cell parameter. More generally, impurities are ascribed to reduce the pressure and temperature needed for phase-transition.[49] Therefore it can be inferred that the dopants increase the strain in the lattice, leading to the reduction in the cell parameter. This could reduce the pressure required for β to γ phase transition, as reported in previous experimental observations.[43] Moreover, the HSE calculation elicits the ineffective role of dopant from the absence of intermediate states by doping. On the contrary, the experimental studies show exaggerated absorption spectra with respect to doping. So, it is still an open question, whether the correlation effect or the structural transition plays a decisive role in the introduction of intermediate band states.

So we have attempted to give a quantitative conclusion for the phase transition based on the calculated free energy as supporting evidence for the above-said experimental phase transition. Moreover the present study explores the presence of an intermediate band by Ti/V doping In_2S_3. In addition, a comparative study to find the critical doping concentration, their influence in the electronic structure, and the energy barrier associated with the structural transition with respect to all polymorphs of In_2S_3 is underway, and will be published elsewhere.

Although a few studies are available on doping the β-In_2S_3, they have not considered the structural transition of doped β-In_2S_3. It is better to look into the impurity substituted γ-In_2S_3 rather than β-In_2S_3. Therefore we have put substantial effort into doping the trigonal (γ) phase of In_2S_3 with different charge states of Ti and V. Formation energy has been calculated for various charge states to check whether the defect structure is stable. We made a detailed analysis on the electronic structure to understand the nature of the IB introduced by the respective impurity. We have also introduced the HSE calculation for the hyper doped system along with spin polarization, in order to take into account the role of the correlation effect on the dispersion of IB.

2 Computational details

The Vienna *Ab initio* simulation package (VASP) was used for the total-energy calculations to study structural stability and to extract the equilibrium structural parameters.[50,51] The projected augmented wave (PAW) method and Perdew, Burke, and Ernzerhof (PBE)[52] parameterization of pseudo-potentials have been adopted to treat the core-valence electron interactions and exchange–correlation functional, respectively. A plane-wave basis set of 550 eV, and $4 \times 4 \times 2$ *k*-point sampling was used for Brillouin zone integration. For suitable repetition of primitive cell a super cell of 60 atoms has been built. However, the defect–defect interaction is not effective for the hexagonal lattice since $r_1 = \frac{\sqrt{3}}{\sqrt{2}a_0}$ and $Z_1 = 12$. For charged defect, the neutralizing background charge has been added. To provide accurate band gap results, hybrid-DFT was employed for the unit cell calculation incorporating 25% screened Hartree–Fock exchange (HSE06 functional).[53] In order to place the IB introduced by the dopant accurately, we carried out the band-edge correction by taking the E_g from the HSE functional. For calculating the defect formation energy, dilute doping ($TM_{0.08}In_{1.92}S_3$) by the supercell approach is carried out. The size of the super cell is selected in such a way that the formation energy is not affected by more than the allowed error value. Usually dilute doping leads to intermediate states, whereas hyper-doping is suggested for forming the IB. Therefore, after careful analysis of the position of intermediate states inside the E_g, the doping concentration has been increased to achieve

a potential IB. To ensure superior agreement of our results with experimental findings, the spin-polarization has also been included in structural relaxation schemes, wherever required.

3 Results and discussion

3.1 Structural relaxation and defect formation energy

The crystal structures of the α and β-phase of In_2S_3 are given in Fig. 1. β-In_2S_3 is the well-known thermodynamically stable phase with ordered vacancies in the defect spinel structure (space group: $I41/amd$).[34] γ-In_2S_3 takes a defect-Th_3P_4 type structure in the $R\bar{3}c$ space group (formula unit; $Z = 6$) with In^{3+} cation occupying 88.89% of 12(a) sites randomly and sulfur anions at the 16(c) sites, without any ordering of the vacancies.[38] Indeed, the intrinsic defects have favorable bonding stability. The C_{3d} point group symmetry of the structure results in three different equatorial bond lengths as shown in Fig. 2a.

The formation energy for the most studied β-In_2S_3 and the new γ-In_2S_3 has been calculated. The heat of formation energy of β-In_2S_3 is −2.74 eV f.u.$^{-1}$ and that for γ-In_2S_3 is −2.63 eV f.u.$^{-1}$. As the β-phase is lower in energy by only 0.11 eV compared to the γ phase, easy structural transition from β to γ phase is evidenced. In general, Gibbs free energy given by $G = U + PV$ defines the total energy (U) for a particular pressure (P) at volume (V). Herein, the Gibbs free energy at zero pressure is −20.6 eV for the γ-In_2S_3 phase.

Fig. 2c shows the relative Gibbs free energy between the β and γ phases of In_2S_3 as a function of pressure. It shows that both the β and γ phases co-exist at 2 GPa indicating that the phase transition would occur at 2 GPa. However, the reported experimental transition pressure (6.6 GPa) is higher than the theoretically observed value. Further, before starting the defect calculation, the lattice parameters have been optimized in the equilibrium volume and fitted to the Birch–Murnaghan equation of state to find the lowest energy configuration (Fig. 2b). These optimized structural parameters are used to build the super cell.

Though the β-In_2S_3 crystal structure consists of octahedral (O_d) and T_d sites for the In atom, the transition metal dopants prefer to substitute those In-sites at O_d positions. The transition metals Ti and V are substituted for the In atoms at the O_d sites in the supercell. The energy required to form In vacancies is 2.341 eV. For the γ-In_2S_3, only the octahedrally coordinated In sites are available for substitution.

The lowest formation energy configuration is shown in Fig. 2d. The formation energy of different defects in various charge states was calculated using the formula.[54]

$$\nabla H^{\mathrm{def}}(q) = E^{\mathrm{tot}}_{\mathrm{def}} - E^{\mathrm{tot}}_{\mathrm{bulk}} \pm \sum_i n_i\mu_i + q[E_{\mathrm{VBM}} + \mu_e] \qquad (1)$$

where $E^{\mathrm{tot}}_{\mathrm{def}}$ and $E^{\mathrm{tot}}_{\mathrm{bulk}}$ are the free energy of the ion–electron configuration of the defect and bulk systems, respectively. The charge neutrality is ensured by setting a homogeneous background charge. The relative stability of the impurity in various charge states with respect to the neutral charge state are shown in Fig. 2d. (The defect formation energy is shown in the ESI Fig. S1†.) The defect states represented by 1+, 0, and 1− correspond to the Ti^{2+}, Ti^{3+} and Ti^{4+} oxidation states, respectively. Similarly, the defect states represented by 1+, 0, 1−, and 2− charges belong to the V^{2+}, V^{3+}, V^{4+}, and V^{5+} oxidation states, respectively.

Both Ti and V substituents are stable in the 1+ charge state in γ-In_2S_3. The 1+ charge state becomes neutralized when the E_F is close to 0.25 eV above the VBM. So by manipulating the synthesis conditions it is possible to stabilize the dopants in the preferred oxidation state. When the E_F is close to the VBM (p-type condition), both Ti and V have lower formation energy for donor states (*i.e.*, 1+ charge state). On the contrary, acceptor type Ti^{1-}_{In}, V^{1-}_{In} and V^{2-}_{In} are stable when E_F is close to the CBM (n-type condition). It can be noted that XPS studies on Fe-substituted In_2S_3 reveal the Fe peaks coming from Fe^{2+} and Fe^{3+} oxidation states (*i.e.*, +1 and neutral charge states).

The E_F is pinned at 0.437 eV with the co-existence of 1+ and 1− charge states of V_{In}. This may occur due to the reduction of V^{2-}_{In} into V^{1-}_{In} and V^{1+}_{In}. This aligns with the co-existence of V^{1-}_{In} (25%) and V^{0}_{In} valence states observed experimentally.[43] Further, the structure is hyper-fine because of the mixed valence states. The elongation of octahedra to fit the defect inside the O_d site may be the reason for reducing the valence state.

The vanadium substituent follows two defect transition paths (i) V^{1+}_{In} and V^{0}_{In}, (ii) another defect path can be followed as V^{1+}_{In}–V^{1-}_{In}–V^{2-}_{In} states. In the latter, the defect transition study

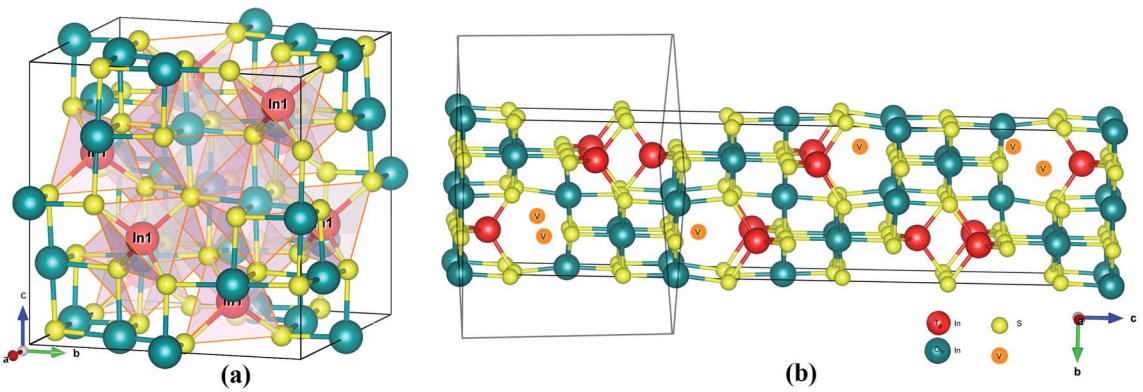

Fig. 1 Crystal structures of (a) α-In_2S_3 and (b) β-In_2S_3.

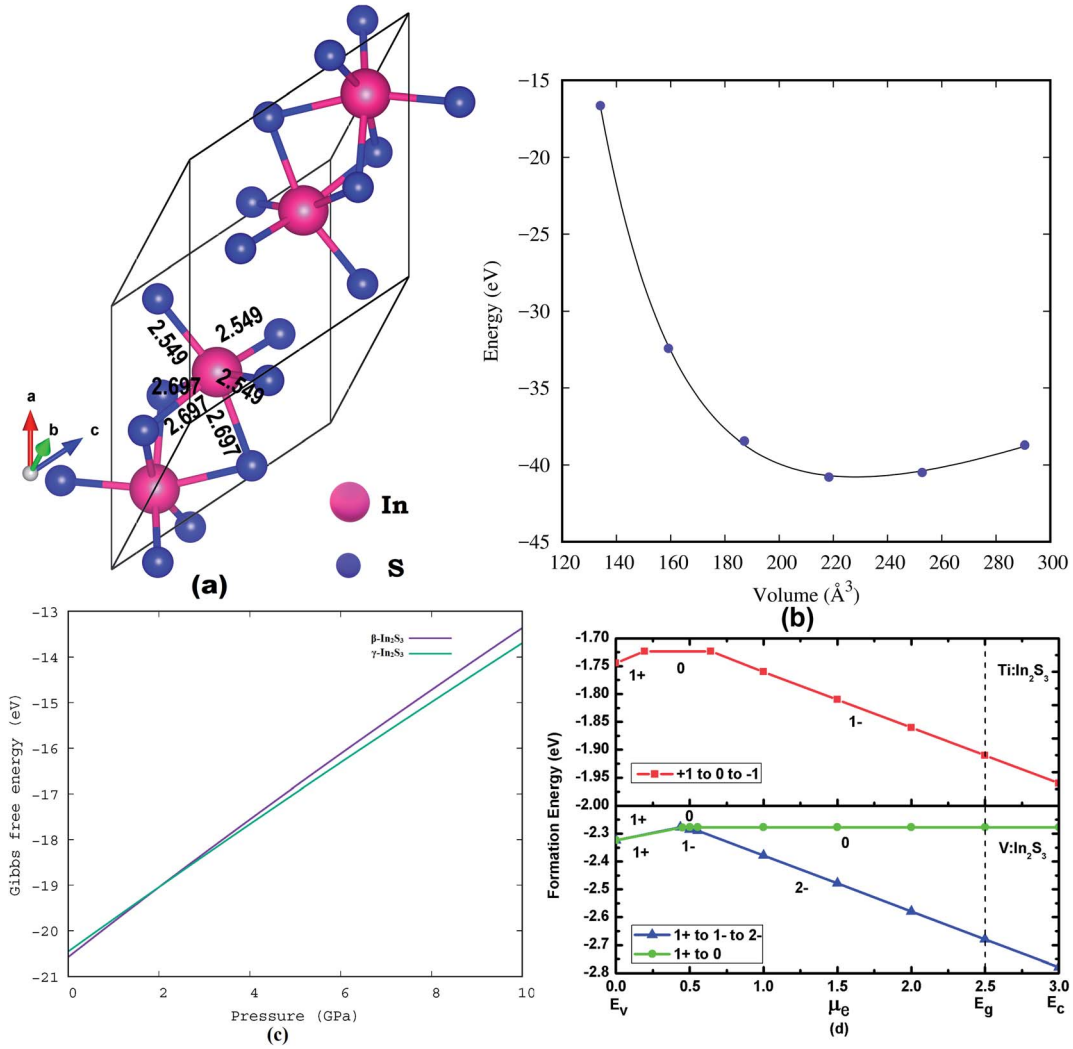

Fig. 2 Crystal structures of (a) γ-In_2S_3, (b) total energy *vs.* volume for γ-In_2S_3, (c) Gibbs free energy of γ-In_2S_3 and (d) defect formation energy of Ti:In_2S_3, and V:In_2S_3.

shows that the second possibility has a direct transition of 1+ charged state to 1− state. In turn, overestimation of electron–phonon coupling takes place, thereby two electrons become attractive (negative-*U*). This observation indicates that the lattice experiences more vibration when transition of defect states takes place, which is reflected in the bond length. Moreover, the reduction of V_{In}^{2-} into V_{In}^{1+} is impractical since it needs a reducing agent like Li or Na *etc.*[55] Hence the defect charge states 0/(neutral), 1− and 2− have the maximum thermodynamic probability to occur. This indicates that a charge transition occurs in the embedded dopant changes, when the Fermi energy is 0.5 eV. The triple donar impurity Ti_{In}^{0} and V_{In}^{0}, become favorable through thermal energy.

Our results lend support to the spontaneous formation of defects since all the charge states have negative formation energy. The finding here is that thermal energy can assist charged defects rather than neutral defects. Hence, the O_d coordination of Ti_{In}^{1-}–S, and V_{In}^{2-}–S, seem to be quite unsuccessful. This means that defects with lower oxidation states fit better to occupy the O_d symmetry sites than those with higher oxidation state. Furthermore, the transition from p-type to n-type conductivity is imminent for Ti:In_2S_3 and V:In_2S_3 near the VBM.

3.2 Electronic properties

In order to find out the favorable defects, reasonable effort has been made to analyze the complete electronic structure of the pure and doped γ-In_2S_3. Depending on the stabilization of the charge state of the impurities, the geometric and electronic structures become modified. First, the E_g of intrinsic γ-In_2S_3 has been calculated by the highly accurate HSE functional which is found to be 2.5 eV (Fig. 3a). Usually the HSE functional gives E_g close to that of experimental values; however, the experimental E_g value is not available for γ-In_2S_3 for comparison.[41] A broad shift in the band gap from 2.15 to 2.50 eV is observed upon the structural phase change from β to γ-In_2S_3. This shows that a small difference in total energy of the β and γ phases induces a huge distinction within the band gap and band features. The

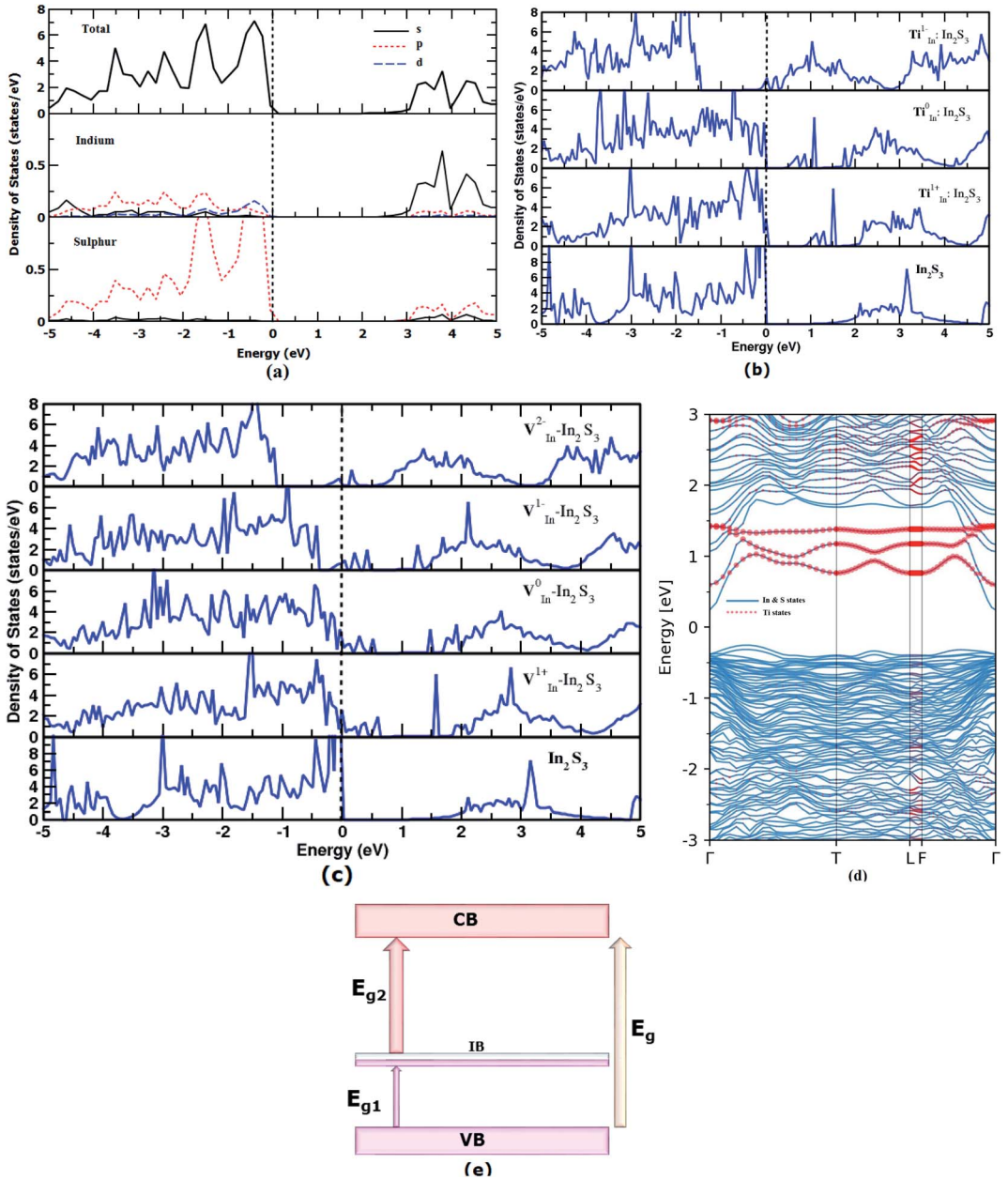

Fig. 3 Density of states of (a) pure γ-In_2S_3 (b) Ti:In_2S_3, and (c) V:In_2S_3. (d) Electronic band structure of Ti^0_{In}:In_2S_3 and (e) illustration of the possible multi-transitions in an intermediate band semiconductor.

partial density of states (pDOS) shows that the valence band maximum (VBM) is contributed to by the hybridized In-d and S-p states. The conduction band minimum (CBM) has predominant In-s states. In order to find the implications of Ti and V dopants and their charge states, on the electronic structure, the total DOS plots are given in Fig. 3b and c.

In Fig. 3b and c, the total DOS of pristine γ-In_2S_3 are given in the lowest panel for comparison. The other panels illustrate the DOS plots of the substituted Ti and V atoms in different charge states. Herein, the new bands introduced between the VBM and CBM are called intermediate bands (IB) represented by total bandgap E_g, lower bandgap E_{g1} and higher bandgap of E_{g2}. These are located in different positions within E_g based on the electronic state of the defects.

The Ti^{1-}_{In} does not introduce any IB whereas Ti^{0}_{In} and Ti^{1+}_{In} give rise to IB at ≈0.5 and ≈1 eV above the VBM, respectively. Hence these two later defects introduce three different band gaps (E_g) into the single semiconductor band gap. Thus, the Ti-doped γ-In_2S_3 can embody the IB which promotes a direct transition of electrons from the VB → IB, IB → CB and VB → CB. In a way, it helps in the effective utilization of a single incident photon to promote three excitations.

The band structure of the Ti^0_{In} defect state has been plotted along the high symmetry points (Fig. 3d). There is a significant state starting from 0.5 eV which pertains to the TM-d orbital

electron. The intermediate states are highlighted in the electronic structure plot. It depicts the intermediate band of moderate width rather than discrete defect levels. The fat band analysis throws more light on the origin of the IB due to Ti_{In}, *viz.*, the d_{xy}, d_{z^2}, and $d_{x^2-y^2}$ orbitals constitute to the IB seen from 0.5 to 1.5 eV, whereas the d_{xz}, d_{yz} orbitals are contributing to the lower unoccupied states of the CB (given in ESI Fig. S2†).

Previous experimental studies stated that the lower energy photons are not absorbed and hence excitations from VBM to lower IB are not seen. If the IB is close to the conduction band it may enhance the possibility for the second gap transition. In this viewpoint, the 'Ti' substitution moves the potential IB position close to the conduction band.

In the case of V substitution at the indium site, the intermediate states fall in the E_F for the V_{In}^{1-} and V_{In}^{2-} charge states. The IB seems to be a partially filled band the same as that of the V_{In} in the tetragonal β-In_2S_3. An interesting feature called the pseudo-gap is observed in the neutral state (V_{In}^{0}) of the defect close to the vicinity of E_F (0 eV), further implicating the partial occupancy of IB. The effect of V_{In} on the electronic structure of β-In_2S_3 and γ-In_2S_3 is similar using the PBE functional.

Fat band analysis shows that for V_{In}^{0} substituted γ-In_2S_3, the orbitals d_{xy}, d_{z^2}, $d_{x^2-y^2}$ form ground state t_{2g} states, and the d_{xz}, d_{yz} orbitals form the e_g states (not shown here). It is worthwhile noting that the intermediate bands introduced by Ti and V substitution are well dispersed. Moreover, the dispersion of bands that were close to the VBM in undoped In_2S_3 increases after the Ti/V substitution. This makes the material suitable for potential photovoltaic applications.[58]

The position of the intermediate band solely depends on the electron count in the valence shell which is reflected in the DOS plot. Further, the intermediate band is placed in close proximity to the valence band.

3.3 Effect of hyper-doping

3.3.1 Bonding analysis. Normally, the IB resulting from a low concentration of dopants can act as a trapping site and hence decrease the number of free charge carriers. On the other hand, a high concentration of dopants can create an intermediate band which will assist in three photon absorption, resulting in enhanced efficiency.[57] Besides, the electron–electron screening effect is anticipated to influence the splitting of d orbitals in the impurity atoms. In addition, the partial occupancy of d-orbitals of Ti and V can lead to a finite atomic magnetic moment. To account for this, we have included a spin-polarized calculation. Also, the electron correlation effect has been taken into account by including hybrid functionals for various high doping concentrations. Experimentally a sub-band gap absorption was found[55,56] for the V concentration of 22.5%. In an effort to mimic this doping limit, we have modelled $TM_xIn_{2-x}S_3$ ($x = 0.5$).

The optimized bond lengths of Ti, V–S and the total energy with respect to the VBM are given in the Table 1, providing information about the distortion induced by the added substituent. The In is surrounded by six sulfur atoms with octahedral co-ordination which contains the rarely observed

Table 1 The bond lengths obtained after structural optimization. Experimental values are given in parentheses

			Bond length (Å)	
Compound	Charge state	Atom	(3×)	(3×)
Pure In_2S_3	Neutral	In–S	2.549 (2.513) (ref. 41)	2.697 (2.746)
Ti:In_2S_3	Ti_{In}^{1-}	In–S	2.534	2.747
		Ti–S	2.429	2.531
	Ti_{In}^{0}	In–S	2.406	2.876
		Ti–S	2.229	2.574
	Ti_{In}^{1+}	In–S	2.351	2.807
		Ti–S	2.174	2.505
V:In_2S_3	V_{In}^{2-}	In–S	2.539	2.725
		V–S	2.424	2.446
	V_{In}^{1-}	In–S	2.411	2.756
		V–S	2.216	2.471
	V_{In}^{0}	In–S	2.359	2.907
		V–S	2.092	2.391
	V_{In}^{1+}	In–S	2.363	2.614
		V–S	2.295	2.534

two pairs of trigonal planar arrangements. Here, the Ti–S bond length decreases in the order Ti_{In}^{1-}–S > Ti_{In}^{0}–S > Ti_{In}^{1+}–S, in which Ti exists in Ti^{4+}, Ti^{3+}, and Ti^{2+} states, respectively. This implies that the Ti_{In}^{1+}–S defect forms the strongest covalent bonds with its S neighbours compared to the other two defects. Also, the ELF value of 0.7 clearly shows the polar covalent nature of the just mentioned bonds. This could explain the stabilization of the Ti_{In}^{1+}–S defect complex, in spite of less electrons being transferred from Ti to the In–S lattice.

However, the bond length of the V substituent site follows the order: V_{In}^{2-}–S > V_{In}^{1+}–S > V_{In}^{1-}–S > V_{In}^{0}–S, where V exists in V^{5+}, V^{2+}, V^{4+}, and V^{3+} states, respectively. This result aligns with the experimental study,[19] showing that the V substituent takes up the V^{3+} state. The bonding analysis shows that the lower oxidation states of V increase the stability by enhancing the covalent interaction with a shorter bond length. The reduction in bond length experienced by the V^{3+}-dopant explains the dominant covalent bonding nature which relaxes atoms inward towards the dopant, compared to the other defect states. Further, the increase in bond length is observed for the V^{2+} substituent which however reduces the stability of the structure relative to the neutral case.

The electron localization function (ELF) yields visual information about the chemical bond in an easily understandable way. It depicts the 3D view of the paired electron distribution. The mapping of electron pair probability for the TM_{In}^{0} doped In_2S_3 is given in Fig. 4. The electron pair density $\eta(r)$ has a proportionality relationship with the electron density ($\log \rho(r)$). Hence the electron density becomes maximum nearer the cation than ionic sulfur. An isosurface value of 0.7 is set to the above mentioned system to identify the difference in the electron pair distribution. The quite high value of ELF (0.7) isosurface lobes are close to the TM sites, implying the polar covalent nature of bonds. The electron localization is a kind of closed loop geometry around the Ti/V–S bonds. The sulfur atom shared by In and Ti has more ELF value and un-symmetric distribution of ELF compared to other S atoms.

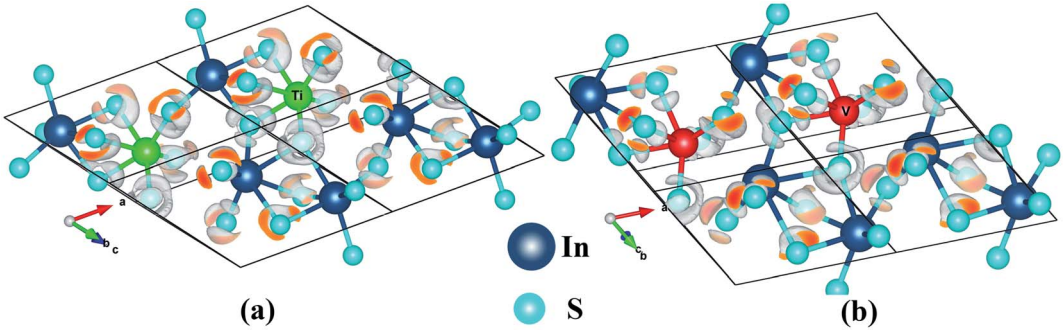

Fig. 4 3D visualization of electron pair localization for ($R\bar{3}c$ type): (a) Ti^{0}_{In}:In_2S_3 (b) V^{0}_{In}:In_2S_3.

The ELF is closer to Ti than that of V which illustrates the influence of d-electrons of the dopants on the distortion of the surrounding octahedra. Furthermore, the vanadium has much more distorted octahedral coordination for the 'V' substitution.

3.4 Density of states

A total density of states and the spin-resolved, atom-projected DOS are shown in Fig. 5a for the Ti^{0}_{In}:In_2S_3 (the same is given in ESI Fig. S3† for charged dopants). The heavily substituted $In_{1.5}Ti_{0.5}S_3$ has an E_g of 3.5 eV. The bonding electronic states of '3d' Ti, and V, clearly manifest the formation of an intermediate band. The sub-band gap E_{g1} starts at 1.5 eV above E_F and spreads up to 3.1 eV. This results in three different energy gap values of E_g = 3.5 eV, E_{g1} = 1.2 eV and E_{g2} = 0.4 eV (refer to Fig. 3e). This indicates the complete change in electronic structure due to the doping concentration beyond the saturation limit.

However, the V^{0}_{In}:In_2S_3 shows E_g similar to the undoped In_2S_3. The IB appearing in $V_{0.5}In_{1.5}S_3$ extends from 0.6 eV above E_F to 2.2 eV inside the band gap of 2.8 eV. Therefore, the entire visible light radiation can be absorbed. The optimum band position has been observed for $V_{0.5}In_{1.5}S_3$ and it is similar to the experimental observation.[43]

In Fig. 5, the additional intermediate bands lie above E_F, contrary to the previous theoretical work, where the completely occupied IB was observed. The completely filled IB can only indulge in the IB → CB transition. Then the material performance would be same as that of the un-doped semiconductor. For instance, if the band is completely filled, the e^-–h^+ pair generation is the same as that of an intrinsic semiconductor since the IBSC would have the IB isolated from the electrical contact. Thereby, the possibility of achieving two e^-–h^+ pair becomes interdependent and may be possible by the following steps: (i) the E_{g2} sub-band photon should promote an e^- from the IB to the CB (refer to Fig. 3e); (ii) simultaneously, the E_{g1} sub-band photon would excite an e^- from the VB to the IB to fill the hole created by the just-mentioned process. Therefore it can create an e^-–h^+ pair in addition to the e^-–h^+ pair introduced by the semiconductor gap (E_g). In our case, the un-filled IB can accommodate and promote an e^- after the first irradiation. In fact, the present results validate the experimental observation of sub-band absorption by allowing three transitions. The overall experimental results have no significant evidence for V_{In}^{-2} states. So it might be reduced to lower oxidation states.

Because of the D_{4d} symmetry of tetragonal β-In_2S_3, the d-band further splits into t_{2g} and e_g sub-shells, thereby causing overlapping of the lower energy states (t_{2g}) with the VBM, and higher energy states (e_g) with the CBM. This precludes the formation of IB.[48] However due to the C_{3d} symmetry of the trigonal γ-In_2S_3 consisting of the trigonally elongated octahedra, where the d-orbitals do not split as in the above scheme. This results in the formation of IB by Ti and V doping in γ-In_2S_3 as shown in Fig. 5. The corresponding d-orbital DOS of the impurity atoms (Ti and V) are given in Fig. 5c and d.

The Ti-d electron sharing the S-p orbital is ascribed to its spin alignment with the S-p orbital. A remarkable observation for this Ti dopant is the formation of an IB with E_g 1.2 eV which is the ideal band gap required for maximum absorption. It seems there is an irregular hybridization of t_{2g} and e_g states in the higher energy region. There is a strong hybridization of the p orbital of In and S along with the d states of Ti in the energy range −3 to −2.5 eV. This implies the neighboring octahedral In interaction in addition to the ligand interaction. For Ti^{0}_{In}, the d^1-electron is distributed evenly among the t_{2g} (d_{xz}, d_{yz}, and d_{xy}) orbitals.

For a given oxidation state, the occupancy of a particular d-orbital depends upon the degree of octahedral distortion. As the S-p orbital receives electrons from In, it has completely filled states. The doped Ti-3d states are predominantly seen in the −2.5 to −3.0 eV range (Fig. 5a).

For an electrically neutral charge state for V substituents, a geometric distortion is observed with compressed trigonal structure. Here, the octahedral distortion is quite high compared to the other valence state of V substitution. Hence, the next nearest neighbouring atomic bonds and angles become very flat along the distorted direction. These ions are expected to be susceptible to angular distortions, to accommodate the impurity in different charge states. Apparently, the geometry becomes planar. This results in energetic degeneracy of d_{xy}, d_{yz} and $d_{x^2-y^2}$ orbitals as the t_{2g} ground state. Then, e_g states are contributed by d_{xz} and d_{z^2} orbitals which are almost empty in the VB. In addition, the states are hybridized to the S-p and In-p orbitals and may provide good bonding properties of solids.

It is shown in Fig. 5e that a narrow, intermediate band is introduced as a result of hyper doping. According to our

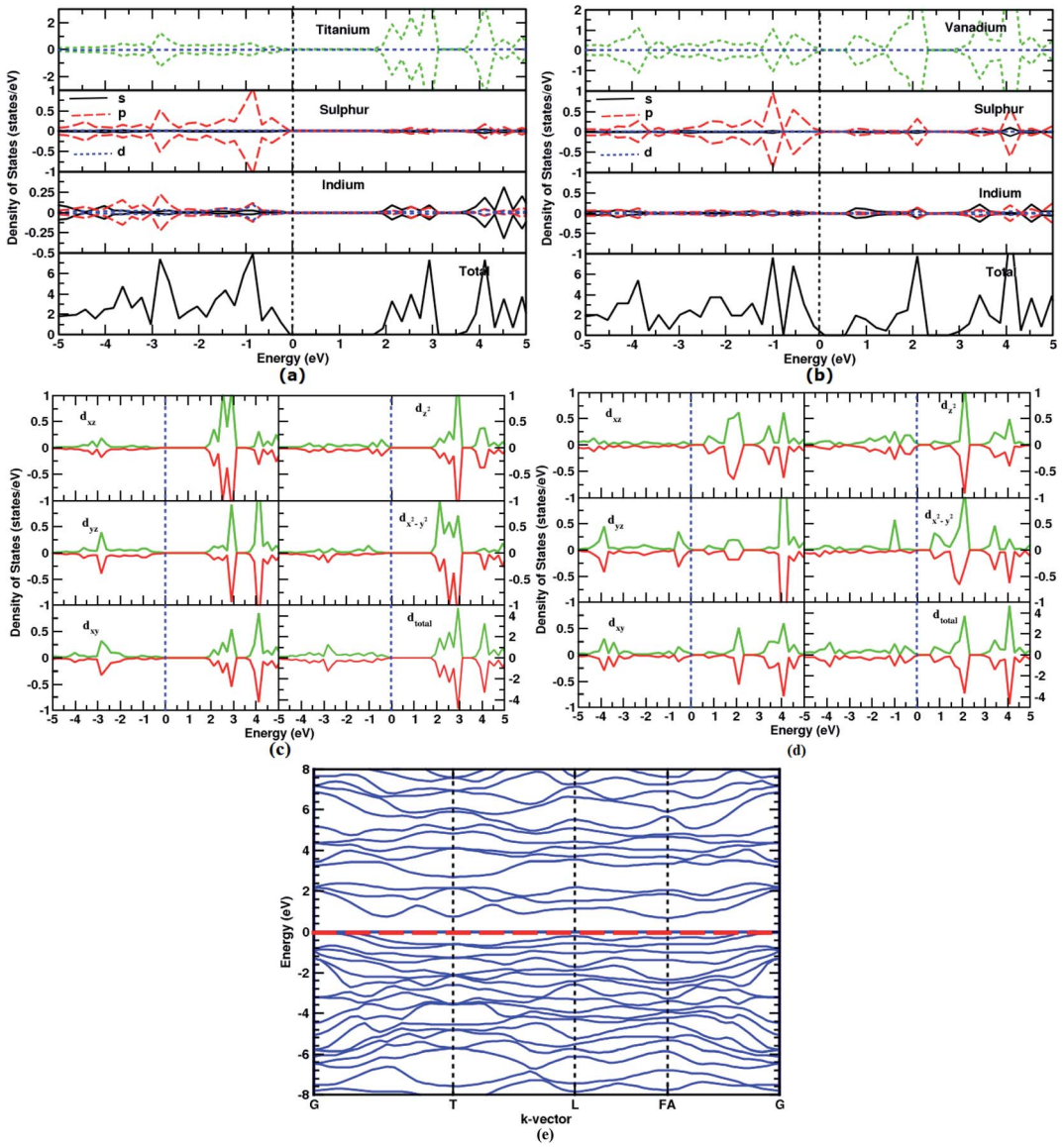

Fig. 5 Spin-resolved density of states of (a) Ti^{0}_{In}:In_2S_3 (b) V^{0}_{In}:In_2S_3, the d-orbital projected DOS for (c) Ti in Ti^{0}_{In}:In_2S_3, (d) V in V^{0}_{In}:In_2S_3, and (e) band structure of V^{0}_{In}:In_2S_3.

findings, the intermediate band region is completely empty. So, it can be useful for photoemission of electrons from the VB to the IB, and the IB to the CB, in addition to direct VB to CB transitions. Herein, it can assist in two step absorption by allowing photons in the energy range, 0.6 eV, 2.2 eV and 2.8 eV, respectively, to the E_g, E_{g1} and E_{g2}. Further the IB to CB has a direct band gap, which can be tuned by varying the doping concentration. Since the IB is less dispersive, the recombination of electrons and holes through this band is not expected to be significantly high.

4 Conclusions

Based on high precision DFT calculations, the structural phase stability of pure In_2S_3 in β and γ variants has been studied. It is found that β-In_2S_3 is the most stable phase being 0.11 eV lower in energy than the γ-phase, and 2 GPa external pressure is sufficient to induce a β to γ phase transition. The experimental structure observed in V-doped In_2S_3 could thus result from the strain induced by the V incorporation. In order to search for the potential intermediate band, we have carried out accurate electronic structure studies using the hybrid functionals. All possible charge states of the dopant atoms were also taken into consideration. Isolated intermediate states are identified within the primary energy gap upon dilute and hyper doping of γ-In_2S_3, which is the new room-temperature polymorph. Ti^{0}_{In} and V^{0}_{In} defects are inferred as the influential defects with IB residing above the Fermi level (E_F). It can be noted that IB can be brought down below the E_F by perturbing the equilibrium either by irradiation or by filling with oxidizing agents. The transition metal induced emphatic IB in γ-In_2S_3 is well placed to notch up enhanced photon absorption. Either way, the conclusions do

stimulate further interest for choosing the right semiconductor phase by tuning the controlled growth mechanism to have the desired valence state of the TM dopant.

Conflicts of interest

There are no conflicts to declare.

Acknowledgements

The author R. Mariyal Jebasty is grateful to the Centre for Research, Anna University, Chennai for offering the Anna Centenary Research Fellowship (Lr. No. CR/ACRF/2017/41) and would like to thank the 'NaFuMa' group, the University of Oslo, for the hospitality under the project "Theoretical and Experimental Studies on Functional Materials (TESFun)" funded by the UTFORSK program of the Centre for Internationalizing Education (SIU), Norway (UTF-2017-four-year-10089). Also, the authors thank the Research Council of Norway for the computation time in NOTUR facilities under the NN2875k project.

References

1 A. Luque and A. Martí, *Phys. Rev. Lett.*, 1997, **78**(26), 5014.
2 A. De Vos, *J. Phys. D: Appl. Phys.*, 1980, **13**(5), 839.
3 A. Luque, A. Martí and C. Stanley, *Nat. Photonics*, 2012, **6**(3), 146.
4 M. Xie, B. Cai, Z. Meng, Y. Gu, S. Zhang, X. Liu, L. Gong, X. A. Li and H. Zeng, *ACS Appl. Mater. Interfaces*, 2020, **12**(5), 6074–6081.
5 Z. Xu, J. Wu, Y. Yang, Z. Lan and J. Lin, *ACS Appl. Energy Mater.*, 2018, **1**(8), 4050–4056.
6 L. M. Yang, P. Ravindran, P. Vajeeston and M. Tilset, *J. Mater. Chem.*, 2012, **22**(32), 16324–16335.
7 T. Wang, X. Li, W. Li, L. Huang, C. Ma, Y. Cheng, J. Cui, H. Luo, G. Zhong and C. Yang, *Mater. Res. Express*, 2016, **3**(4), 045905.
8 P. Olsson, C. Domain and J. F. Guillemoles, *Phys. Rev. Lett.*, 2009, **102**(22), 227204.
9 P. Palacios, I. Aguilera, K. Sanchez, J. C. Conesa and P. Wahnón, *Phys. Rev. Lett.*, 2008, **101**(4), 046403.
10 P. Wahnón, P. Palacios, I. Aguilera, Y. Seminovski, J. C. Conesa José and R. Lucena. *25th European Photovoltaic Solar Energy Conference and Exhibition*, 2019, pp. 203–206, DOI: 10.4229/25theupvsec2010-1bo.8.5.
11 P. Wahnón and C. Tablero, *Phys. Rev. B: Condens. Matter Mater. Phys.*, 2002, **65**(16), 165115.
12 C. Tablero, *Sol. Energy Mater. Sol. Cells*, 2006, **90**(5), 588–596.
13 Y. Seminóvski, P. Palacios and P. Wahnón, *Thin Solid Films*, 2011, **519**(21), 7517–7521.
14 C. Tablero, A. J. García, J. J. Fernández, P. Palacios and P. Wahnón, *Comput. Mater. Sci.*, 2003, **27**(1–2), 58–64.
15 I. Aguilera, P. Palacios and P. Wahnón, *Thin Solid Films*, 2008, **516**(20), 7055–7059.
16 I. Aguilera, P. Palacios, K. Sánchez and P. Wahnón, *Phys. Rev. B: Condens. Matter Mater. Phys.*, 2010, **81**(7), 075206.
17 P. Wahnón, J. C. Conesa, P. Palacios, R. Lucena, I. Aguilera, Y. Seminovski and F. Fresno, *Phys. Chem. Chem. Phys.*, 2011, **13**(45), 20401–20407.
18 O. A. Yassin, A. A. Abdelaziz and A. Y. Jaber, *Mater. Sci. Semicond. Process.*, 2015, **38**, 81–86.
19 C. Tapia, S. P. Berglund, D. Friedrich, T. Dittrich, P. Bogdanoff, Y. Liu, S. Levcenko, T. Unold, J. C. Conesa, A. L. De Lacey and M. Pita, *J. Phys. Chem. C*, 2016, **120**(50), 28753–28761.
20 C. Tapia, S. Zacarias, I. A. Pereira, J. C. Conesa, M. Pita and A. L. De Lacey, *ACS Catal.*, 2016, **6**(9), 5691–5698.
21 R. K. Sharma, Y. N. Chouryal, S. Nigam, J. Saravanakumar, S. Barik and P. Ghosh, *ChemistrySelect*, 2018, **3**(28), 8171–8182.
22 Y. Gao, S. Zhang, X. Bu and Y. Tian, *Catal. Today*, 2019, **327**, 271–278.
23 R. Jayakrishnan, C. S. Kartha and K. P. Vijayakumar, *Mater. Sci. Semicond. Process.*, 2011, **14**(1), 58–61.
24 Y. Li, Y. Gao, N. Xiao, P. Ning, L. Yu, J. Zhang, P. Niu, Y. Ma and C. Gao, *AIP Adv.*, 2018, **8**(11), 115202.
25 Y. X. Chen, K. Kitahara and T. Takeuchi, *J. Appl. Phys.*, 2015, **118**(24), 245103.
26 L. Mohammed, A. M. Isa, A. Musa, T. Mahmood and M. A. Saeed, *Chalcogenide Lett.*, 2016, **13**(1).
27 L. Bhira, H. Essaidi, S. Belgacem, G. Couturier, J. Salardenne, N. Barreaux and J. C. Bernede, *Phys. Status Solidi A*, 2000, **181**(2), 427–435.
28 K. S. Kambas, J. Spyridelis and M. Balkanski, *Phys. Status Solidi B*, 1981, **105**(1), 291–296.
29 M. I. Naher, F. Parvin, A. K. Islam and S. H. Naqib, arXiv:1706.03314, 2017, 11.
30 https://materialsproject.org/materials/mp-22216/.
31 E. D. Jemmis, K. T. Giju and J. E. Leszczynski, *Electron. J. Theor. Chem.*, 1997, **2**(1), 130–138.
32 B. A. Andersson, *Prog. Photovoltaics Res. Appl.*, 2000, **8**(1), 61–76.
33 R. O. Diehl, C. D. Carpentier and R. Nitsche, *Acta Crystallogr., Sect. B: Struct. Crystallogr. Cryst. Chem.*, 1976, **32**(4), 1257–1260.
34 P. Pistor, J. M. Merino Álvarez, M. León, M. Di Michiel, S. Schorr, R. Klenk and S. Lehmann, *Acta Crystallogr., Sect. B: Struct. Sci., Cryst. Eng. Mater.*, 2016, **72**(3), 410–415.
35 H. Hahn and W. Klingler, *Z. Anorg. Chem.*, 1949, **260**(1–3), 97–109.
36 K. Range and M. Zabel, *Z. Naturforsch., B: Anorg. Chem., Org. Chem.*, 1978, **33**, 463–464.
37 X. Lai, F. Zhu, Y. Wu, R. Huang, X. Wu, Q. Zhang, K. Yang and S. Qin, *J. Solid State Chem.*, 2014, **210**(1), 155–159.
38 K. Liu, L. Dai, H. Li, H. Hu, L. Yang, C. Pu and M. Hong, *Chem. Phys.*, 2019, **524**, 63–69.
39 Y. Sharma and P. Srivastava, *Mater. Chem. Phys.*, 2012, **135**(2–3), 385–394.
40 H. B. Abdallah and R. Bennaceur, *Phys. B*, 2006, **382**(1–2), 181–188.
41 F. Horani and E. Lifshitz, *Chem. Mater.*, 2019, **31**(5), 1784–1793.

42 I. Aguilera, P. Palacios and P. Wahnón, *Phys. Rev. B: Condens. Matter Mater. Phys.*, 2011, **84**(11), 115106.
43 R. Lucena, I. Aguilera, P. Palacios, P. Wahnón and J. C. Conesa, *Chem. Mater.*, 2008, **20**(16), 5125–5127.
44 L. A. Wagele, D. Rata, G. Gurieva and R. Scheer, *Phys. Status Solidi C*, 2017, **14**(6), 1600204.
45 Y. Xu, H. Zhu, C. Ma, P. Zhu, R. Cong, X. Wu, W. Gao and Q. Cui, *J. Solid State Chem.*, 2013, **202**, 33–37.
46 Y. Wang, Y. Zhang, W. J. Chang, G. L. Lu, J. Z. Jiang, Y. C. Li, J. Liu and T. D. Hu, *J. Phys. Chem. Solids*, 2005, **66**(10), 1775–1778.
47 L. Wu, T. Hou, Y. Wang, Y. Zhao, Z. Guo, Y. Li and S. T. Lee, *J. Alloys Compd.*, 2012, **541**, 250–255.
48 E. Ghorbani, P. Erhart and K. Albe, *J. Mater. Chem. A*, 2019, **7**(13), 7745–7751.
49 R. G. Hennig, D. R. Trinkle, J. Bouchet, S. G. Srinivasan, R. C. Albers and J. W. Wilkins, *Nat. Mater.*, 2005, **4**(2), 129.
50 G. Kresse and J. Hafner, *Phys. Rev. B: Condens. Matter Mater. Phys.*, 1993, **47**(1), 558.
51 G. Kresse and D. Joubert, *Phys. Rev. B: Condens. Matter Mater. Phys.*, 1999, **59**(3), 1758.
52 J. Perdew, K. Burke and M. Ernzerhof, *Phys. Rev. Lett.*, 1996, **78**, 1396.
53 J. Heyd, G. E. Scuseria and M. Ernzerhof, *J. Chem. Phys.*, 2003, **118**(18), 8207.
54 R. Vidya, P. Ravindran, H. Fjellvag, B. G. Svensson, E. Monakhov, M. Ganchenkova and R. M. Nieminen, *Phys. Rev. B: Condens. Matter Mater. Phys.*, 2011, **83**(4), 045206.
55 R. F. McCarthy, M. S. Weimer, R. T. Haasch, R. D. Schaller, A. S. Hock and A. B. Martinson, *Chem. Mater.*, 2016, **28**(7), 2033–2040.
56 R. F. McCarthy, M. S. Weimer, A. S. Hock, and A. B. Martinson, *IEEE 40th Photovoltaic Specialist Conference (PVSC)*, 2014, vol. 8, pp. 0250–0253.
57 A. Luque, A. Marti, E. Antolin and C. Tablero, *Phys. B*, 2006, **382**(1–2), 320–327.
58 M. I. Lee, A. Barragán, M. N. Nair, V. L. Jacques, D. Le Bolloc'h, P. Fertey, K. Jemli, F. Lédée, G. Trippé-Allard, E. Deleporte and A. Taleb-Ibrahimi, *J. Phys. D: Appl. Phys.*, 2017, **50**(26), 26LT02.